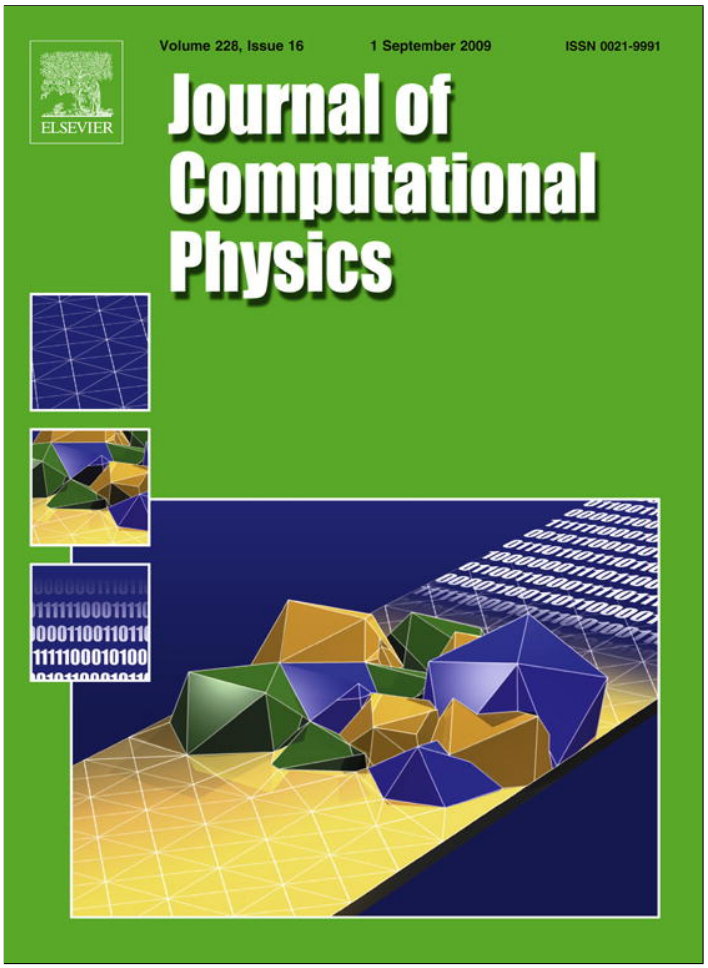

Journal of Computational Physics 228 (2009) 5917–5932

Contents lists available at ScienceDirect

Journal of Computational Physics

journal homepage: www.elsevier.com/locate/jcp

Finite difference computation of acoustic scattering by small surface inhomogeneities and discontinuities

Christopher K.W. Tam *, Hongbin Ju

Department of Mathematics, Florida State University, Tallahassee, FL 32306-4510, United States

ARTICLE INFO

Article history:
Received 24 December 2008
Received in revised form 29 April 2009
Accepted 4 May 2009
Available online 15 May 2009

Keywords:
Computational acoustics
Acoustic scattering
Surface discontinuity
Surface inhomogeneity
Spurious reflected waves

ABSTRACT

The use of finite difference schemes to compute the scattering of acoustic waves by surfaces made up of different materials with sharp surface discontinuities at the joints would, invariably, result in the generations of spurious reflected waves of numerical origin. Spurious scattered waves are produced even if a high-order scheme capable of resolving and supporting the propagation of the incident wave is used. This problem is of practical importance in jet engine duct acoustic computation. In this work, the basic reason for the generation of spurious numerical waves is first examined. It is known that when the governing partial differential equations of acoustics are discretized, one should only use the long waves of the computational scheme to represent or simulate the physical waves. The short waves of the computational scheme have entirely different propagation characteristics. They are the spurious numerical waves. A method by which high wave number components (short waves) in the wave scattering process is intentionally removed so as to minimize the scattering of spurious numerical waves is proposed. This method is implemented in several examples from computational aeroacoustics to illustrate its effectiveness, accuracy and efficiency. This method is also employed to compute the scattering of acoustic waves by scatterers, such as rigid wall acoustic liner splices, with width smaller than the computational mesh size. Good results are obtained when comparing with computed results using much smaller mesh size. The method is further extended for applications to computations of acoustic wave reflection and scattering by very small surface inhomogeneities with simple geometries.

1. Introduction

In computational aeroacoustics, one is often required to compute acoustic reflections from surfaces made up of different materials. At the junction of two materials, such as shown in Fig. 1, the incident sound waves encounter a line discontinuity. Computationally, the grid size is, inevitably, finite. Because of the finite size mesh, experience indicates that spurious reflected waves are usually produced. To minimize spurious reflected waves, it is necessary to use a very fine computational mesh. This is sometimes a very costly remedy. One objective of this work is to devise a method to minimize such spurious reflected waves without having to refine the computational mesh.

In jet engines, acoustic liners are, invariably, installed on the inside surface of inlet and exhausted ducts, (see Motsinger and Kraft [1] and Eversman [2]). Acoustic liners are the most effective device for engine fan noise suppression at the present time. The junction between two acoustical liners with different impedance are examples of surface discontinuity. To facilitate the installation and maintenance of acoustic liners, hard wall splices are introduced. These splices are installed between

* Corresponding author. Tel.: +1 850 644 2455; fax: +1 850 644 4053.
E-mail address: tam@math.fsu.edu (C.K.W. Tam).

0021-9991/$ - see front matter © 2009 Elsevier Inc. All rights reserved.
doi:10.1016/j.jcp.2009.05.005

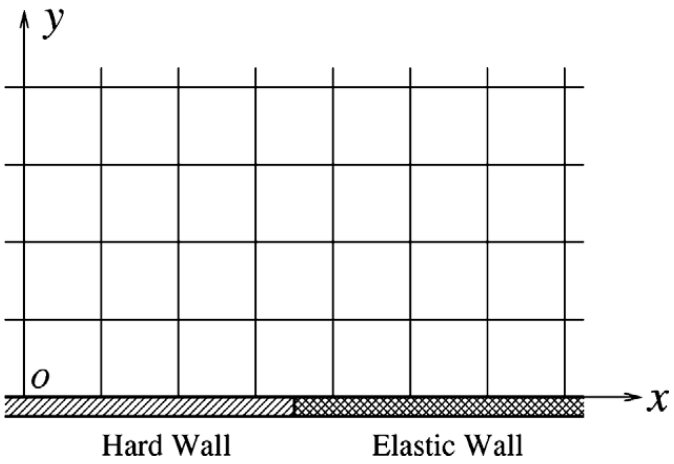

Fig. 1. Discontinuity at the junction of two surface materials. Also shown is the computational mesh.

two pieces of acoustic liners. Their presence creates additional surface discontinuities. In a duct, the continuous reflection of acoustic waves from the wall leads to the formation of coherent propagating wave entities called duct modes or acoustic modes. They were first found by Tyler and Sofrin [3] and have been the subject of numerous studies (Refs. [4–8]) since. The presence of hard wall splices causes the scattering of the duct modes generated by the rotating fan blades of the engine. The scattered duct modes would, inevitably, include lower order spinning azimuthal modes. The lower order modes are not as heavily damped by the acoustic liner. This results in higher level of radiated noise from the engine. This is extremely undesirable. To minimize scattering of duct modes by hard wall splices, engine manufacturers resort to the use of very narrow splices. This poses a real dilemma for duct mode computation. In the absence of narrow splices the use of a computational mesh with 7 to 8 mesh points per wave length in conjunction with a large stencil high-order computational aeroacoustic (CAA) algorithm will have enough resolution for the computation. However, with narrow splices, the splice width is sometimes less than the size of a mesh spacing. This is as shown in Fig. 2. In this case, the hard wall splice is invisible to the computation. Traditional wisdom will call for the use of much finer mesh. A factor of 10 or more mesh size reduction is often deemed necessary. This is to allow 8 to 10 mesh points to lie on the hard wall splice. This is, undoubtedly, very expensive. Not only the number of grid points has to increase substantially, the size of the time step used in the computation also has to be significantly reduced. Another objective of this investigation is to propose a method to perform the narrow splice scattering computation using the original coarse grid without mesh size reduction.

The rest of this paper is as follows. The basic idea of how to compute acoustic reflection from surfaces with discontinuities and small surface features using a coarse mesh is discussed in Section 2. We shall call the method the "wave number truncation" method. Numerical examples illustrating the effectiveness of this method are presented in Section 3. Section 4 is devoted to the computations of acoustic reflection from two-dimensional small surface inhomogeneities. Section 5 summarizes and concludes this paper.

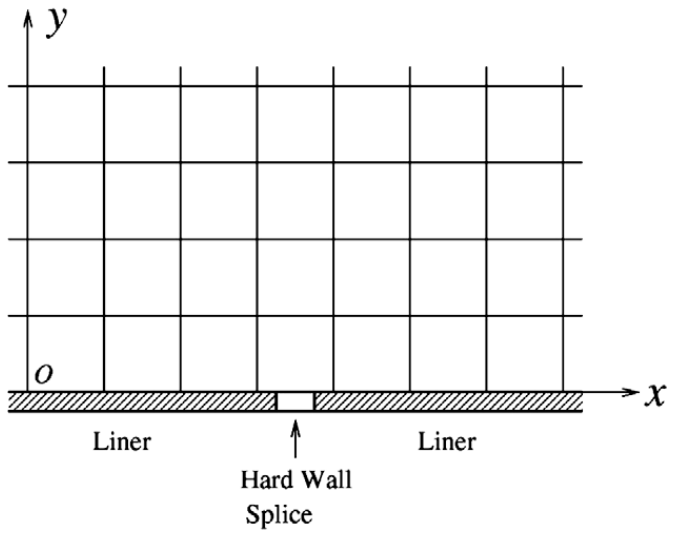

Fig. 2. A narrow splice with width smaller than a grid spacing.

2. The basic idea of wave number truncation method

The proposed method involves the elimination of high wave number in a wall boundary condition. Thus, some understanding of the concept of wave number of a finite difference scheme is essential. Because of this need, we will begin with a brief review of the properties of a finite difference scheme in wave number space.

It is now known, e.g. Tam and Webb [9], Tam [10] and others that the resolution and wave propagation characteristics supported by a finite difference scheme may be analyzed in wave number space. In computing the propagation of acoustic waves, a large stencil central difference scheme is favored. Such a scheme has high resolution and no numerical dissipation. Consider the use of a $(2N+1)$ size central difference quotient to approximate a partial derivative; i.e.,

$$\left(\frac{\partial f}{\partial x}\right)_{\ell} \approx \frac{1}{\Delta x}\sum_{j=-N}^{N} a_j f_{\ell+j}, \tag{1}$$

where subscript l indicates the mesh index and Δx is the mesh size (see Fig. 3). Although Eq. (1) is meant to apply only to the set of grid points shown in Fig. 3, we will, nevertheless, generalize this finite difference relation and apply it to every set of points spaced at Δx apart on the x-axis. The generalized finite difference approximation for a continuous variable x is

$$\frac{\partial f(x)}{\partial x} \approx \frac{1}{\Delta x}\sum_{j=-N}^{N} a_j f(x+j\Delta x). \tag{2}$$

When x is equal to $\ell\Delta x$, that is x is located at a stencil point, Eq. (2) is identical to Eq. (1).

Let $\tilde{f}(\alpha)$ be the Fourier transform of $f(x)$, then $f(x)$ and $\tilde{f}(\alpha)$ are related by

$$\tilde{f}(\alpha) = \frac{1}{2\pi}\int_{-\infty}^{\infty} f(x)e^{-i\alpha x}dx; \quad f(x) = \int_{-\infty}^{\infty}\tilde{f}(\alpha)e^{i\alpha x}d\alpha.$$

The Fourier transform of Eq. (2), using the Shifting Theorem, is,

$$i\alpha\tilde{f} \approx i\bar{\alpha}\tilde{f}, \tag{3}$$

where

$$\bar{\alpha}\Delta x = \sum_{j=-N}^{N} a_j e^{ij\alpha\Delta x}. \tag{4}$$

The α on the left side of Eq. (3) is the true wave number. Thus $\bar{\alpha}$ on the right side of Eq. (3) is effectively the stencil wave number of the finite difference approximation. This was noted by Tam and Webb [9]. $\bar{\alpha}\Delta x$ is a periodic function of $\alpha\Delta x$. Fig. 4 shows the fundamental period with $-\pi < \alpha\Delta x < \pi$. Outside the fundamental period, the waves have wavelength less than two mesh spacings. They are unresolved by the computation scheme. These ultra-short waves are aliased back into the fundamental period. They are pollutants of the numerical computation.

In Fig. 4, the line $\bar{\alpha}\Delta x = \alpha\Delta x$ represents the exact approximation. Shown in this figure also is the $\bar{\alpha}\Delta x$ as a function of $\alpha\Delta x$ relationship for the 7-point stencil Dispersion-Relation-Preserving (DRP) scheme [9]. It is typical of all high-order finite difference scheme. Marked on this curve is the break point $\alpha_c\Delta x$ at which the finite difference approximation starts to deviate substantially from the exact approximation. The value of $\alpha_c\Delta x$ depends on the particular finite difference scheme. $\alpha_c\Delta x$ marks the upper limit of waves for which the computation scheme can resolve accurately. The short waves with $\alpha > \alpha_c$ are waves that cannot be accurately resolved by the scheme. Furthermore, the short waves do not propagate at the correct wave speed. For the very short waves with wave number lying on the part of the $\bar{\alpha}\Delta x - \alpha\Delta x$ curve with a negative slope, they propagate in a direction opposite to that of the long waves. Ideally, the short waves as well as the ultra-short waves should be removed from the computation. Here they are referred to as spurious waves.

Now consider the wall boundary condition shown in Fig. 1. On the hard wall side of the junction, the rigid wall boundary condition is,

$$v = 0 \tag{5}$$

where v is the velocity component normal to the wall. Let κ be the elastic constant of the elastic wall and ζ be the vertical displacement of the surface (positive in the direction of outward pointing normal) then the elastic wall boundary condition is

$$\zeta = -\kappa(p - p_{ref}) \tag{6}$$

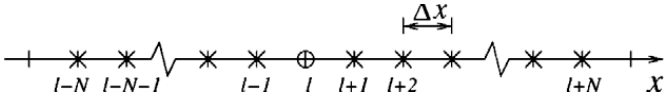

Fig. 3. A $(2N+1)$ size central difference stencil.

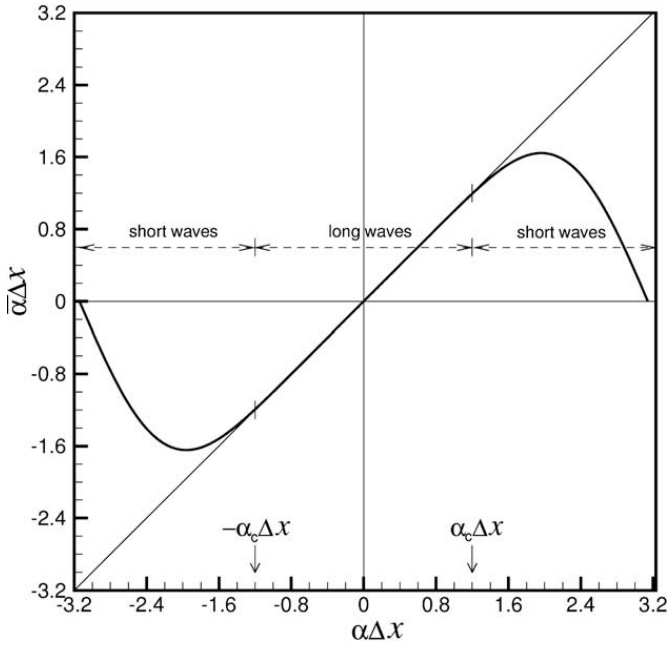

Fig. 4. The fundamental period of finite difference schemes.

where p is the pressure and p_{ref} is the reference pressure for zero displacement. By differentiating Eq. (6) with respect to time, t, it is found,

$$\frac{\partial \zeta}{\partial t} = v = -\kappa \frac{\partial p}{\partial t}. \tag{7}$$

Boundary conditions (5) and (7) may be combined into a single boundary condition by means of the unit step function, $H(x)$. Let the wall junction be at $x = 0$, then the unified boundary condition at the wall is

$$v = -\kappa \frac{\partial p}{\partial t} H(x). \tag{8}$$

It is useful to consider the boundary condition (8) in wave number space. The Fourier transform of Eq. (8) is,

$$\tilde{v}(\alpha) = -\frac{\kappa}{2\pi} \int_{-\infty}^{\infty} \tilde{H}(\alpha - k) \frac{\partial \tilde{p}}{\partial t}(k) dk. \tag{9}$$

The right side of Eq. (9) is a convolution integral. The Fourier transform of the unit step function is

$$\tilde{H}(\alpha) = -\frac{i}{2\pi\alpha}. \tag{10}$$

Thus $\tilde{H}(\alpha)$ involves all wave numbers including wave numbers in the short and ultra-short waves number range of the computational scheme. The convolution integral of Eq. (9) would, therefore, generate wave numbers outside the long wave range. In other words, because $\tilde{H}(\alpha)$ contains spurious waves with respect to the computational scheme, the surface discontinuity would scatter off spurious waves in an acoustic wave reflection computation.

A way to minimize the generation of spurious waves is to remove all the wave numbers in the short and ultra-short wave number range of $\tilde{H}(\alpha)$; i.e., wave number higher than the cut-off. Thus a modified boundary condition is to replace $\tilde{H}(\alpha)$ by $\tilde{H}(\alpha)[H(\alpha + \alpha_c) - H(\alpha - \alpha_c)]$ in Eq. (9) where α_c is the cut-off wave number. In physical space, this is tantamount to replacing $H(x)$ in Eq. (8) by $\hat{H}(x)$ where $\hat{H}(x)$ is the inverse Fourier transform of $\tilde{H}(\alpha)[H(\alpha + \alpha_c) - H(\alpha - \alpha_c)]$; i.e.,

$$\hat{H}(x) = \int_{-\infty}^{\infty} -\frac{i}{2\pi\alpha}[H(\alpha + \alpha_c) - H(\alpha - \alpha_c)] e^{i\alpha x} d\alpha = \frac{1}{2} + \frac{1}{\pi} Si(\alpha_c x). \tag{11}$$

In Eq. (11), the $Si(z)$ function is defined as (see Abramowitz and Stegun [11] (Chapter 5, Section 5.2)),

$$Si(z) = \int_0^z \frac{\sin(y)}{y} dy. \tag{12}$$

Fig. 5 shows $\hat{H}(x)$ as a function of $\alpha_c x$. Now, we propose to use the following modified boundary condition instead of the exact boundary condition (8)

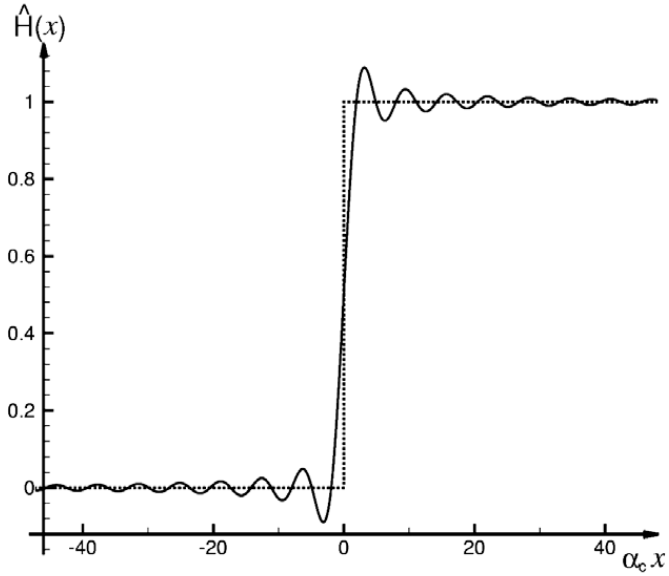

Fig. 5. The $\hat{H}(x)$ function.

$$v = -\kappa \frac{\partial p}{\partial t} \hat{H}(x). \tag{13}$$

That is, we replace $H(x)$ by $\hat{H}(x)$. We shall call the above method the wave number truncation method. The effectiveness and accuracy of this method and its extension will be demonstrated by several examples in the next section.

3. Numerical examples

In this section, three numerical examples are presented to illustrate the effectiveness and accuracy of the wave number truncation method. These examples have practical relevance to jet engine duct acoustics. The inlet duct of a jet engine generally has a nearly circular geometry. The inside surface is covered by an acoustic liner. The liner occupies the space between two hard wall surfaces. One hard wall surface is the metallic surface surrounding the fan of the engine. The other hard wall surface is the lip of the engine inlet. The purpose of the acoustic liner is to damp out as much as possible the acoustic waves in the form of duct modes generated by the rotating fan. The duct modes propagate from the fan face upstream against the flow. They are radiated out from the inlet. A simplified model of the inlet duct is shown in Fig. 6. This model has been used by numerous investigators for computing duct/acoustic mode propagation in jet engine ducts; e.g. Regan and Eaton [12], McAlpine et al. [13], Tester et al. [14] and Tam et al. [15]. Due to a number of practical reasons, it is a standard practice to install hard wall splices to separate a liner into smaller pieces. Two types of splices are used. The more common type is the axial splice. An axial splice runs along the entire length of the liner. Fig. 7 shows an inlet duct with two axial splices. Instead of axial splices, circumferential splices are often used. These splices form a ring around the inside surface of the duct. A duct with a circumferential splice is shown in Fig. 8.

Recently, it is recognized that the presence of liner splices leads to the scattering of the upstream propagating duct modes into other modes (see Ref. [14,15]). Some of the scattered modes are not as heavily damped by the liner as the original incident duct mode because of their different modal structures. On reaching the inlet of the engine, the scattered modes become the dominant modes. This increases the radiated noise. This is most objectionable. To reduce duct mode scattering, very thin splices are used. In the examples below, a mesh spacing that is sufficiently accurate for computing the incident acoustic modes is used. The mesh spacing is, however, wider than the width of an axial splice (see Fig. 2). It will be shown that such computations can be carried out with good accuracy by means of the wave number truncation method.

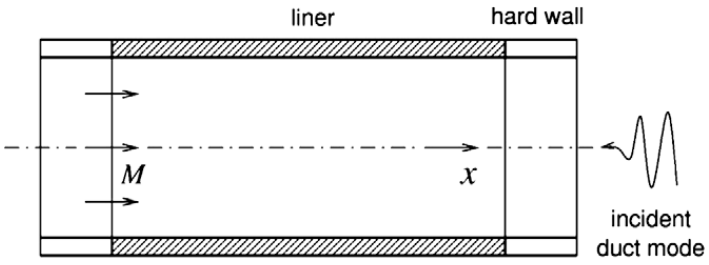

Fig. 6. A computational model of the inlet duct of a jet engine.

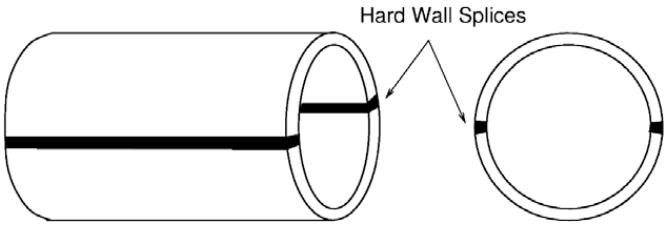

Fig. 7. Computational model of an inlet duct with two axial splices.

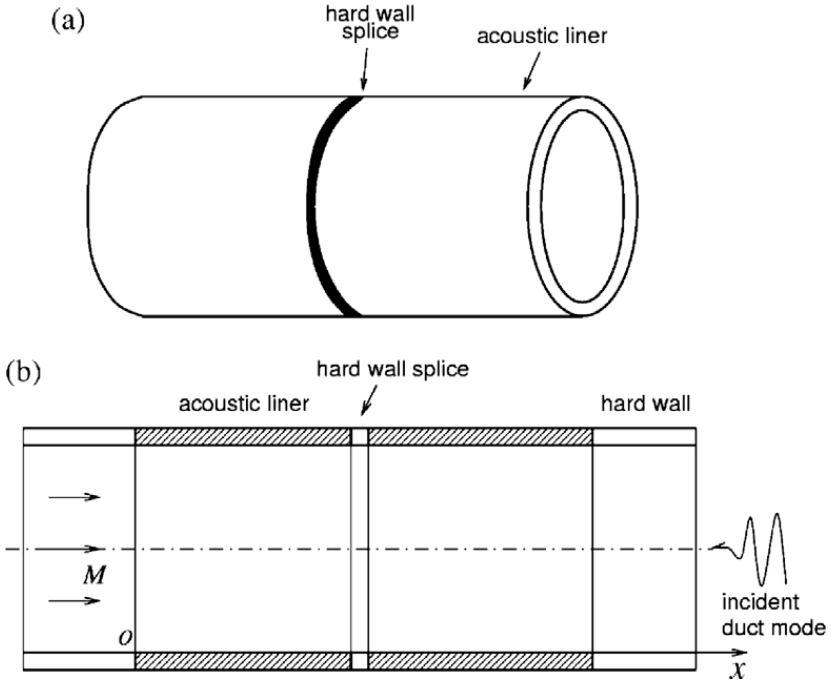

Fig. 8. Computational model of an inlet duct with a circumferential splice.

Acoustic liners are characterized by an impedance $Z = R - iX$ ($e^{-i\Omega t}$ time dependence assumed) where R is the resistance and X is the reactance. For time marching computation, the liner is modelled by a time domain impedance boundary condition. Time domain impedance boundary condition is a topic that has been studied by a number of investigators (Tam and Auriault [16], Ozyoruk et al. [17], Fung and Ju [18], Botteldooren [19], Zheng and Zhuang [20], Li et al. [21], Rienstra [22], Ju and Fung [23] and Reyman et al. [24]). Here we will adopt the formulation of Tam and Auriault. The dimensionless liner surface boundary condition for a liner with a given R and X in a grazing flow of Mach number M is

$$R\frac{\partial v}{\partial t} - X_{-1}v + X_1\frac{\partial^2 v}{\partial t^2} = \frac{\partial p}{\partial t} + M\frac{\partial p}{\partial x} \tag{14}$$

where

$$X_1 = \frac{1}{\left[\frac{2}{|Z|} - \frac{X}{|Z|^2}\right]\Omega}, \quad X_{-1} = -\frac{\left(1 - \frac{X}{|Z|}\right)^2\Omega}{\left[\frac{2}{|Z|} - \frac{X}{|Z|^2}\right]}$$

$$X = \frac{X_{-1}}{\Omega} + X_1\Omega, \quad \Omega \text{ is the angular frequency of the upstream propagating duct mode.}$$

Note: length scale D (diameter of duct), velocity scale a_0 (speed of sound), time scale D/a_0, density scale ρ_0 (mean flow density), pressure scale $\rho_0 a_0^2$, impedance scale $\rho_0 a_0$ are used to form dimensionless variables in boundary condition (14) and the rest of Section 3.

3.1. Scattering of acoustic duct mode at the entrance and exit of an inlet duct

At the entrance or the exit of an inlet duct, there is a surface discontinuity at the junction of the liner and hard wall (see Fig. 6). These junctions, invariably, cause significant spurious scattering of a propagating duct mode. The scattering is an

artifact of discrete computation. It can be reduced by using a finer size mesh or by implementing the wave number truncation method.

The governing equations of motion of the gas inside an inlet duct are the linearized dimensionless Euler equations. In cylindrical coordinates, these equations are

$$\frac{\partial \rho}{\partial t} + M\frac{\partial \rho}{\partial x} + \frac{\partial v}{\partial r} + \frac{v}{r} + \frac{1}{r}\frac{\partial w}{\partial \phi} + \frac{\partial u}{\partial x} = 0, \tag{15}$$

$$\frac{\partial v}{\partial t} + M\frac{\partial v}{\partial x} = -\frac{\partial p}{\partial r}, \tag{16}$$

$$\frac{\partial w}{\partial t} + M\frac{\partial w}{\partial x} = -\frac{1}{r}\frac{\partial p}{\partial \phi}, \tag{17}$$

$$\frac{\partial u}{\partial t} + M\frac{\partial u}{\partial x} = -\frac{\partial p}{\partial x}, \tag{18}$$

$$\frac{\partial p}{\partial t} + M\frac{\partial p}{\partial x} + \frac{\partial v}{\partial r} + \frac{v}{r} + \frac{1}{r}\frac{\partial w}{\partial \phi} + \frac{\partial u}{\partial x} = 0, \tag{19}$$

where $M = u/a_0$ is the flow Mach number.

On the duct surface, the hard wall boundary condition is

$$r = \frac{1}{2}, \quad v = 0. \tag{20}$$

On the liner surface, the boundary condition is Eq. (14). At the left hand junction of the computational model (Fig. 6), the hard wall and liner boundary conditions can be combined to form a single boundary condition by means of the unit step function. The combined boundary condition is,

$$R\frac{\partial v}{\partial t} - X_{-1}v + X_1\frac{\partial^2 v}{\partial t^2} = H(x)\left(\frac{\partial p}{\partial t} + M\frac{\partial p}{\partial x}\right). \tag{21}$$

Note: On the hard wall, $x < 0$, the $H(x)$ function of boundary condition (21) is zero. This reduces the right side of the equation to zero. With initial condition $v = \partial v/\partial t = 0$, the only solution is $v = 0$. In implementing the wave number truncation method, boundary condition (21) is replaced by,

$$R\frac{\partial v}{\partial t} - X_{-1}v + X_1\frac{\partial^2 v}{\partial t^2} = \hat{H}(x)\left(\frac{\partial p}{\partial t} + M\frac{\partial p}{\partial x}\right). \tag{22}$$

A cylindrical mesh, as shown in Fig. 9, is used to compute the propagation of acoustic modes upstream from the hard wall region on the right side of the inlet model of Fig. 6 to the left side. A uniform size mesh in the axial direction is used. We will consider an incident duct mode with azimuthal mode number $m = 26$ and radial mode number $n = 1$ and a dimensionless

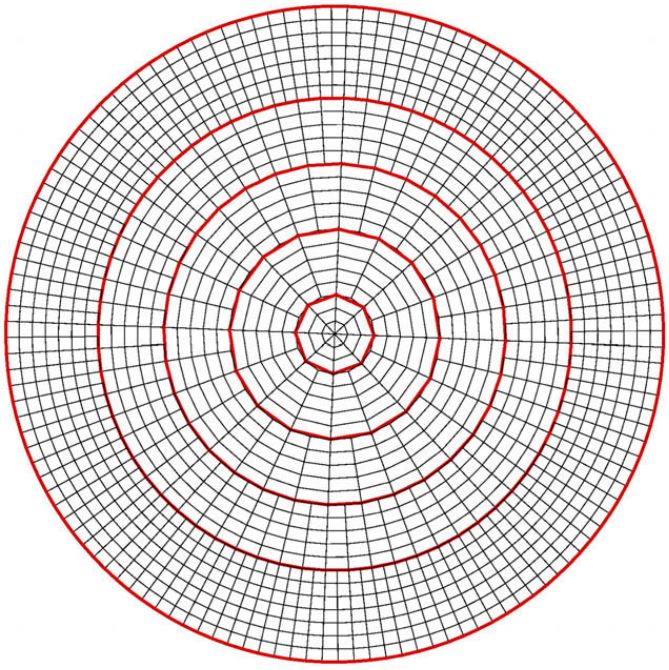

Fig. 9. Cylindrical grid for inlet duct acoustic mode computation. Only half the mesh lines are shown.

angular frequency $\Omega = 57.3$. For such an acoustic mode, an axial mesh with $\Delta x = 0.008$ will allow the computation to have more than 8 mesh points per axial wave length. This is the mesh used in all the computations of this section unless explicitly stated otherwise. In the computation, the 7-point stencil DRP scheme[9] is used to approximate the derivatives. The multi-mesh-size multi-time-step DRP scheme of Tam and Kurbatskii [25] is used to march the solution in time. The duct wall boundary conditions (liner impedance, $Z = 2 + i$, time factor $\exp(-i\Omega t)$) are enforced by the ghost point method [26]. Recently, this method has been used successfully by Tam et al. [15] in their spliced liner study. On the left and right end of the computational domain, a perfectly matched layer (PML), using the methodology of Hu [27,28], is implemented. The PML absorbs all the outgoing waves. The incident acoustic mode, that enters the computational domain on the right side, is introduced into the computation by the split variable method as in the work of Tam et al. [15].

Fig. 10 shows the axial distribution of computed acoustic energy flux (PWL) associated with an incident duct mode with azimuthal mode number 26 and other parameters as stipulated above. PWL is the total energy flux of all the sound waves in the duct. It is defined as,

$$\mathrm{PWL} = \int_0^{2\pi} \int_0^{1/2} \langle (1+M^2)pu + M(p^2+u^2) \rangle r dr d\phi \tag{23}$$

where $\langle\ \rangle$ is the time average. PWL(db) = 10 log (PWL/$\mathrm{PWL}_{\text{incident wave}}$). This form of energy flux was derived by Morfey [29]. Of particular interest to us are the computed results near the left junction between acoustics liner and hard wall. In this region, the effect of scattering of spurious acoustic waves is most severe and easily observable. The full line in this figure is the computed axial distribution of PWL using boundary condition (21) and axial mesh size 0.008. This curve exhibits strong spatial oscillations with wavelength nearly equal to two axial mesh spacings. This is clear evidence of spurious scattering. The dotted line is the same computation but using boundary condition (22). The computed distribution of PWL is smooth and free of spatial oscillations. This indicates that the wave number truncation method is, indeed, capable of removing spurious numerical scattering. To check the accuracy of the computed results by this method, a series of computations using boundary condition (21) is carried out with smaller and smaller axial mesh size Δx. Δx equals to 1/4, 1/8 and 1/16 of the original mesh size are used. The results near the left side liner–hard wall junction are shown in Fig. 11 in an enlarged scale. As can be seen as Δx is reduced, the computed result approaches that using boundary condition (22) but with a much larger Δx. The fact that there is good agreement between results using much smaller Δx and boundary condition (21) and that using boundary condition (22) but much larger Δx is evidence that the spatial oscillations of the full curve is of numerical origin. Further, it shows that the method of wave number truncation is effective and accurate. It also offers large savings in computer memory and CPU time.

3.2. Scattering by very thin axial splices

We will now consider acoustic mode scattering by two thin axial splices. The computational model is shown in Fig. 7. The same computational grid (see Fig. 9) as in the previous subsection is used. The azimuthal mesh size of the outermost ring of the cylindrical mesh is equal to 0.0123. We will consider two hard wall splices with a width of 0.006. So the splice width is

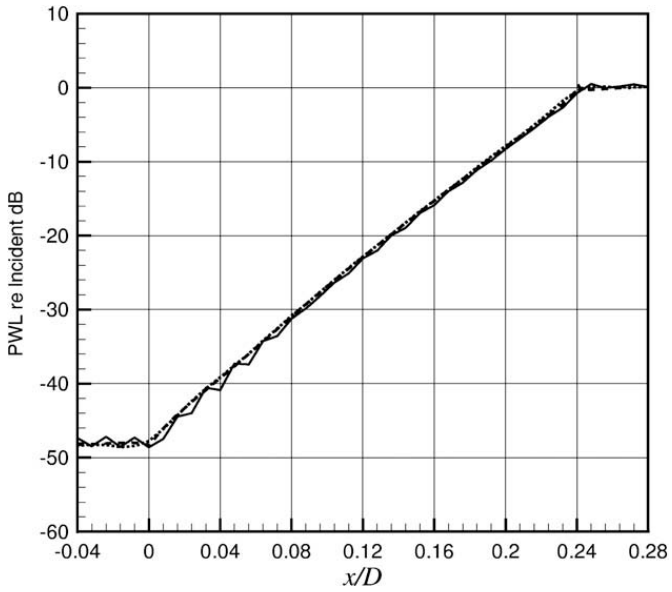

Fig. 10. Axial distribution of PWL. Incident wave has azimuthal mode number $m = 26$, radial mode number $n = 1$, angular frequency $\Omega = 57.3$. Liner impedance $Z = 2 + i$ (time factor $e^{-i\Omega t}$). — computed by boundary condition (21), $\Delta x = 0.008$; ---- computed by boundary condition (21), $\Delta x = 0.001$; ····· computed by boundary condition (22), $\Delta x = 0.008$.

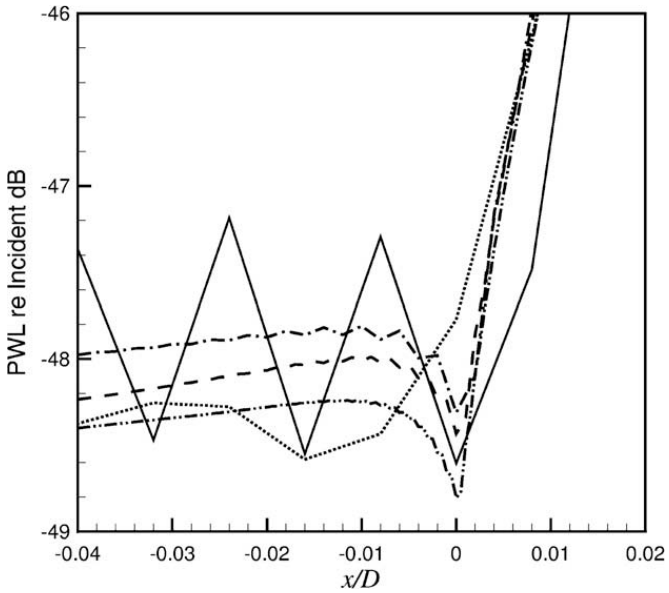

Fig. 11. Enlarged bottom left hand corner of Fig. 10. Computed by boundary condition (21), — $\Delta x = 0.008$,– · – $\Delta x = 0.002$, ---- $\Delta x = 0.001$, –··– $\Delta x = 0.0005$, ····· computed by boundary condition (22), $\Delta x = 0.008$

approximately half of that of the mesh spacing (see Fig. 2). In other words, the splices are invisible to the discretized computation.

Let us introduce a periodic function, $G(\phi)$, of period 2π, defined by,

$$G(\phi) = \begin{cases} 0, & -\frac{\Delta\Phi}{2} < \phi < \frac{\Delta\Phi}{2}, \pi - \frac{\Delta\Phi}{2} < \phi < \pi + \frac{\Delta\Phi}{2} \\ 1, & \text{otherwise} \end{cases} \tag{24}$$

where $\Delta\Phi$ is the angle subtended by a splice. A graph of $G(\phi)$ is shown in Fig. 12. When applied to the surface of the duct, $G(\phi)$ is equal to 1 where there is acoustic liner. It is equal to zero where there is hard wall splice. By means of the G-function, the wall boundary condition in the duct may be written as,

$$R\frac{\partial v}{\partial t} - X_{-1}v + X_1\frac{\partial^2 v}{\partial t^2} = G(\phi)\left[\frac{\partial p}{\partial t} + M\frac{\partial p}{\partial x}\right]. \tag{25}$$

Now $G(\phi)$ is a period function, it may be expanded as a Fourier series. It is easy to find,

$$G(\phi) = \sum_{j=0}^{\infty} a_j \cos(j\phi) \tag{26}$$

where

$$a_0 = \left(1 - \frac{\Delta\Phi}{\pi}\right), a_j = -\frac{2}{\pi j}\left[1 + (-1)^j\right]\sin\left(\frac{j\Delta\Phi}{2}\right), \quad j = 1, 2, 3, \ldots. \tag{27}$$

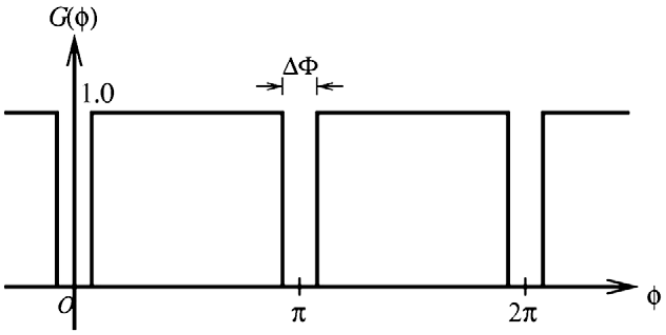

Fig. 12. The periodic $G(\phi)$ function.

It is clear from Fourier expansion (26) that the $G(\phi)$ function contains components that are beyond the resolution of the 7-point stencil DRP scheme. To compute acoustic wave propagation in the duct, these high wave number components essentially make the splice invisible to the computational mesh. To make the spliced liner compatible with the numerical scheme, a simple way is to remove all Fourier components with azimuthal wave length shorter than the cut-off wave length of the computational algorithm. Accordingly, all Fourier components with mode number m larger than m_c, where the wave length of mode m_c is the same as or is closest to the smallest resolved wave length of the computation scheme. For the cylindrical mesh used in the present computation, the azimuthal mesh size at the outermost ring is equal to 0.0123. For the 7-point stencil DRP scheme, $\alpha_c\Delta x = 1.2$, so that $\alpha_c = 1.2/0.0123 = 97.6$. Hence by equating m_c to the integer value closest to $\alpha_c/2$, we find $m_c = 49$. Fig. 13 shows the graph of the truncated Fourier Series, $G(\hat{\phi})$, (Fourier components with m greater than 49 are removed), i.e.

$$\hat{G}(\phi) = \sum_{m=0}^{m_c} a_j \cos(j\phi) \tag{28}$$

The modified spliced liner boundary condition is to replace $G(\phi)$ by $\hat{G}(\phi)$ in Eq. (25), i.e.,

$$R\frac{\partial v}{\partial t} - X_{-1}v + X_1\frac{\partial^2 v}{\partial t^2} = \hat{G}(\phi)\left[\frac{\partial p}{\partial t} + M\frac{\partial p}{\partial x}\right]. \tag{29}$$

Fig. 14 shows three computed PWL distributions along the length of the duct for the same incident duct mode as in the example of Section 3.1. In this computation, boundary condition (22) is used in the neighborhood of the liner–hard wall junction at the two ends of the computational model. The dotted line in Fig. 14 shows the numerical result when boundary

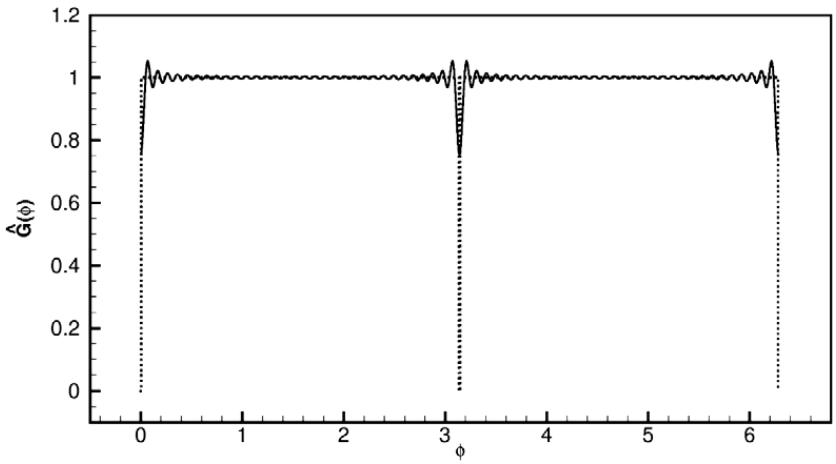

Fig. 13. The periodic $\hat{G}(\phi)$ function.

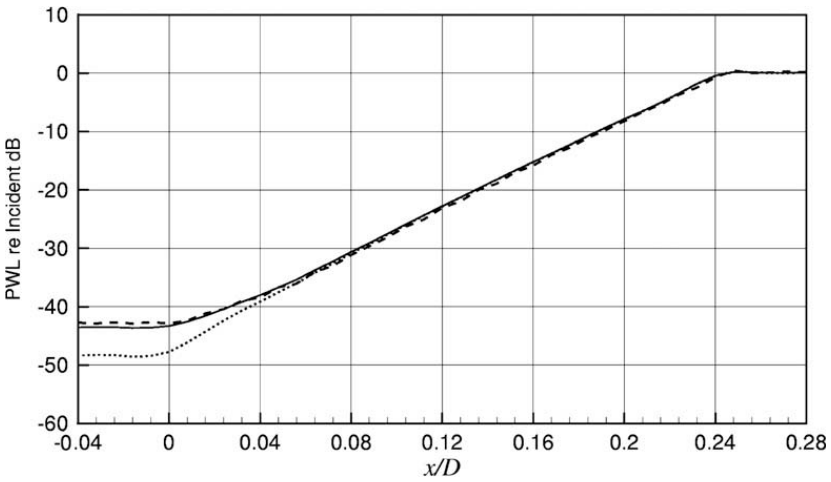

Fig. 14. Axial distribution of PWL. Incident wave has azimuthal mode number $m = 26$, radial mode number $n = 1$, angular frequency $\omega = 57.3$. Liner impedance $Z = 2+i$ (time factor $e^{-i\omega t}$). $\Delta x = 0.008$ — computed by boundary condition (29), ····· computed by boundary condition (25), ---- computed by Fourier expansion method (89 modes) of Ref. [15].

condition (25) is used. There is no scattering in this case as the splices are invisible to the computational mesh. The full line is the computation using modified boundary condition (29). There is a large difference between these two curves. The difference is the energy of the scattered waves that are clearly quite substantial at the duct inlet. To check the accuracy of the wave number truncation method, a third computation using the quasi-two-dimension azimuthal mode expansion method of Tam et al. [15] is carried out. This method expands the propagating acoustic waves in a large number of azimuthal modes. For the present computation, modes up to $(m_c + 40)$ are included. As a result of the large number of modes, the computation requires very large computer memory and long CPU time. The dash curve of Fig. 14 is the computed result using this method. It is evident that the result is very close to that of the wave number truncation method. This example offers a rigorous test of the effectiveness and accuracy of the wave number truncation method for computing the scattering of acoustic waves by narrow scatterers.

3.3. Scattering by thin circumferential splices

In this third example, the scattering of acoustic modes by a circumferential splice is considered. The computational model is shown in Fig. 8. For this test case, the width of the circumferential splices is taken to be $2.5\Delta x$. For this size splice, there are only two mesh points on the splice surface ($\Delta x = 0.008$).

Let us consider a function $F(x)$ defined by,

$$F(x) = \left[H\left(x - x_c + \frac{W}{2}\right) - H\left(x - x_c - \frac{W}{2}\right)\right] \tag{30}$$

where x_c is the location of the center of the splice and W is its width. By means of the $F(x)$ function, the wall boundary condition for a liner with a single circumferential splice may be written as

$$R\frac{\partial v}{\partial t} - X_{-1}v + X_1\frac{\partial^2 v}{\partial t^2} = [1 - F(x)]\left[\frac{\partial p}{\partial t} + M\frac{\partial p}{\partial x}\right]. \tag{31}$$

Now, the Fourier transform of $F(x)$ is,

$$\tilde{F}(\alpha) = \frac{e^{-i\alpha x_c}}{\pi\alpha}\sin\left(\frac{\alpha W}{2}\right). \tag{32}$$

Following the concept of the wave number truncated method, the high wave number components of Eq. (32) are to be removed at this stage. The truncated $\widehat{F}(\alpha)$ function is,

$$\widehat{F}(\alpha) = \frac{e^{-i\alpha x_c}}{\pi\alpha}\sin\left(\frac{\alpha W}{2}\right)[H(\alpha + \alpha_c) - H(\alpha - \alpha_c)]. \tag{33}$$

The inverse of $\widehat{F}(\alpha)$ is easily found to be,

$$\widehat{F}(x) = \frac{1}{\pi}[Si((x - x_c + 0.5W)\alpha_c) - Si((x - x_c - 0.5W)\alpha_c)]. \tag{34}$$

A graph of $\widehat{F}(x)$ is given in Fig. 15. The modified boundary condition to replace Eq. (31) is,

$$R\frac{\partial v}{\partial t} - X_{-1}v + X_1\frac{\partial^2 v}{\partial t^2} = \left[1 - \widehat{F}(x)\right]\left(\frac{\partial p}{\partial t} + M\frac{\partial p}{\partial x}\right). \tag{35}$$

Fig. 16 shows the results of four computations for duct mode scattering by a circumferential splice of width 0.02 located between $x = 0.11$ and 0.13. The incident duct mode and the liner impedance are the same as in the previous two examples. The first three computations use boundary condition (31). The mesh size used in the first computation is $\Delta x = 0.002$. There is spurious acoustic scattering at the upstream end of the splice. The axial distribution of the acoustic PWL is the upper most broken curve in Fig. 16. The second and third computation use a mesh size of $\Delta x = 0.0005$ and 0.00025 respectively. It is clear from this figure that the spurious scattering diminishes with the use of a finer mesh. The fourth computation uses modified boundary condition (35) and a very coarse mesh of $\Delta x = 0.008$. This is 32 times the size of the finest mesh used. For this computation, there are only two mesh points on the splice. The computed axial distribution of PWL is shown as the full line in Fig. 16. For the transmitted PWL, which is one of the important quantities of the duct mode transmission computation, it is clear that the fourth computation using a mesh size 32 times larger gives almost identical result as that of the finest mesh (using the original unmodified boundary condition). This example further illustrates the advantage of the wave number truncation method.

4. Small two-dimensional scatterers

Computation of the scattering of acoustic waves by small two-dimensional surface inhomogeneities will now be investigated. We will limit our consideration to scatterers with a simple geometry. Specifically only the shapes of rectangles and circles are studied.

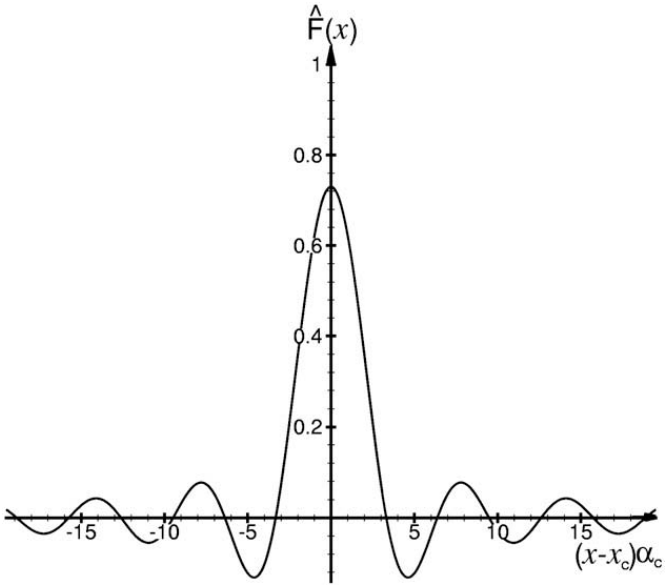

Fig. 15. The $\widehat{F}(x)$ function. $W\alpha_c = 2.5$.

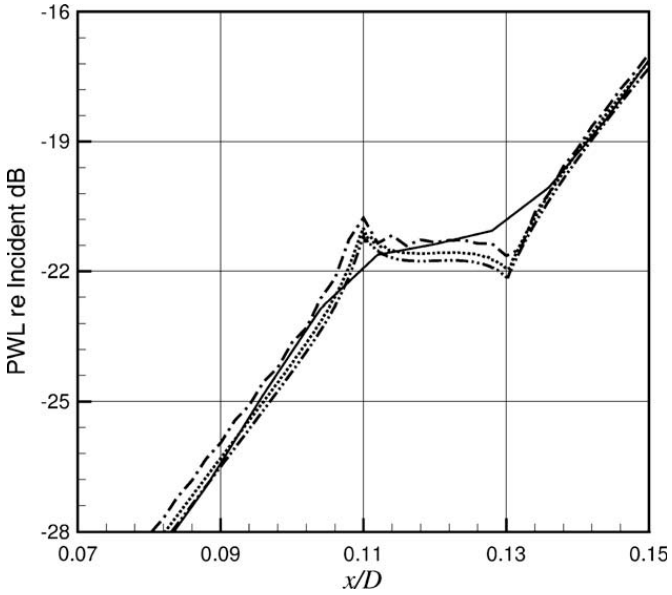

Fig. 16. Duct mode scattering by a circumferential splice of width 0.02. Incident wave mode and liner impedance are the same as Fig. 10. Comparison of transmitted PWL: computed by boundary condition (35) — $\Delta x = 0.008$; the following computed by boundary condition (31), – · – $\Delta x = 0.002$, ····· ·· $\Delta x = 0.0005$, –· ·– $\Delta x = 0.00025$.

4.1. Small rectangles

For a rectangle with a width W in the x-direction and a height B in the y-direction centered at (x_c,y_c) (see Fig. 17), the discontinuous function of the scatterer, $R(x,y)$, is,

$$R(x,y) = \left[H\left(x - x_c + \frac{W}{2}\right) - H\left(x - x_c - \frac{W}{2}\right)\right]\left[H\left(y - y_c + \frac{B}{2}\right) - H\left(y - y_c - \frac{B}{2}\right)\right]. \tag{36}$$

It is easy to show that the Fourier transform of $R(x,y)$ is

$$\tilde{R}(\alpha,\beta) = \frac{e^{-i(\alpha x_c + \beta y_c)}}{\pi^2 \alpha\beta} \sin\left(\frac{\alpha W}{2}\right) \sin\left(\frac{\beta B}{2}\right) \tag{37}$$

where α and β are the Fourier transform variables in x and y.

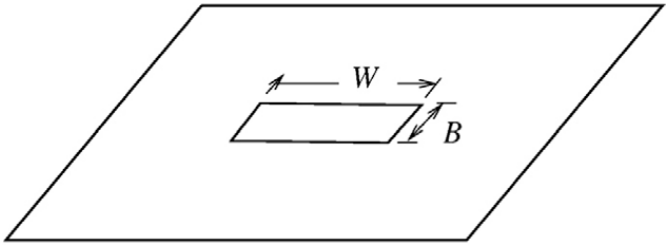

Fig. 17. A two-dimensional scatterer in the form of a rectangle.

The wave number truncated function $\hat{R}$ is,

$$\hat{R}(\alpha,\beta)=\frac{e^{-i(\alpha x_c+\beta y_c)}}{\pi^2\alpha\beta}\sin\left(\frac{\alpha W}{2}\right)\sin\left(\frac{\beta B}{2}\right)[H(\alpha+\alpha_c)-H(\alpha-\alpha_c)][H(\beta+\beta_c)-H(\beta-\beta_c)]. \tag{38}$$

The inverse transform of Eq. (38) is,

$$\hat{R}(x,y)=\frac{1}{\pi^2}\left[Si\left((x-x_c+\frac{W}{2})\alpha_c\right)-Si\left((x-x_c-\frac{W}{2})\alpha_c\right)\right]\left[Si\left((y-y_c+\frac{B}{2})\beta_c\right)-Si\left((y-y_c-\frac{B}{2})\beta_c\right)\right]. \tag{39}$$

It should be straightforward to use $\hat{R}(x,y)$ to develop a modified boundary condition for surface scattering involving inhomogeneities with a rectangular geometry.

4.2. Small circles

For a circle with a diameter D centered at the origin (see Fig. 18), the associated discontinuities function $C(x,y)$ is,

$$C(x,y)=\begin{cases}1, & \text{if } x^2+y^2<\frac{D^2}{4}\\ 0, & \text{otherwise}\end{cases}. \tag{40}$$

The Fourier transform of (40) is,

$$\tilde{C}(\alpha,\beta)=\frac{1}{2\pi^2}\int\int_{\text{circle}}e^{-i(\alpha x+\beta y)}dxdy. \tag{41}$$

To evaluate double integral (41), let us make a change of variables to polar coordinates (r,ϕ) so that,

$$x=r\cos\phi,\quad y=r\sin\phi,\quad \alpha=k\cos\Phi,\quad \beta=k\sin\Phi. \tag{42}$$

In polar coordinates, Eq. (41) becomes,

$$\tilde{C}(k,\Phi)=\frac{1}{(2\pi)^2}\int_0^{\frac{D}{2}}\int_0^{2\pi}e^{-ikr\cos(\phi-\Phi)}rd\phi dr=\frac{1}{2\pi}\int_0^{\frac{D}{2}}J_0(kr)rdr=\frac{D}{4\pi k}J_1\left(k\frac{D}{2}\right) \tag{43}$$

where $J_0(z)$ and $J_1(z)$ are Bessel functions of order zero and one.

On discarding all wave numbers with $k>k_c$ (k_c is the cutoff wave number), the truncated $\tilde{C}$ function is

$$\tilde{C}(k,\Phi)=\frac{D}{4\pi k}J_1\left(k\frac{D}{2}\right)[1-H(k-k_c)]. \tag{44}$$

In physical space, the truncated $C(x,y)$ function is,

$$\hat{C}(r,\phi)=\int_0^{\infty}\int_0^{2\pi}\tilde{C}(k,\Phi)e^{ikr\cos(\phi-\Phi)}kd\Phi dk=\int_0^{k_cD/2}J_1(y)J_0(2yr/D)dy \tag{45}$$

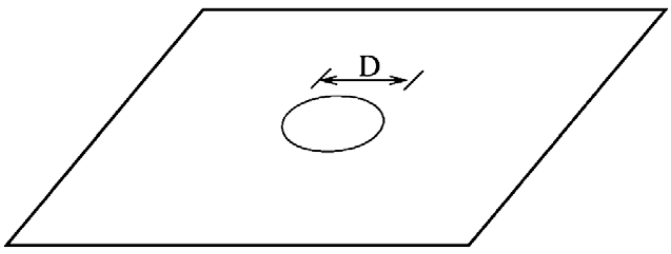

Fig. 18. A two-dimensional scatterer in the form of a circle.

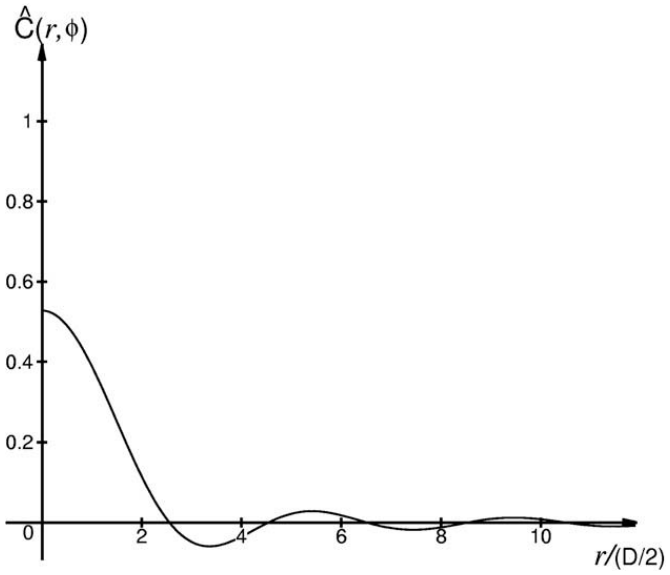

Fig. 19. The $\widehat{C}(r,\phi)$ function, $k_cD = \pi$.

The graph of $\widehat{C}(r,\phi)$as a function of $r/(D/2)$ for $k_cD = \pi$ is shown in Fig. 19. By means of function $\widehat{C}(x,y)$, it is not difficult to establish a modified boundary condition for a small inhomogeneity in the form of a circle.

5. Summary and conclusion

In computing the scattering of acoustic waves by surfaces with material discontinuities, one, invariably, encounters spurious scattering due to the fact that a discretized scheme is used. The scattering is of numerical origin unrelated to the physical problem. The underlying cause of such spurious scattering is that a finite difference scheme has a limited resolved band width in wave number space. A surface discontinuity involves wave numbers of infinite range. Thus wave numbers larger than those that can be supported by the finite difference scheme would be reflected off by a surface with a discontinuity. This produces spurious spatial oscillations in the numerical solution.

In this paper a wave number truncation method is introduced to minimize the spurious reflection. The basic idea of the method is to eliminate all wave numbers larger than the cut-off wave number of the computation scheme. In this way the truncated spectrum is less likely to give rise to spurious numerical scattering.

Three numerical examples of practical significance are presented. They involve surface discontinuities between jet engine acoustic liner and hard metallic wall surfaces. One of the examples involves hard wall splices with a width less than the mesh size used for computation. Without applying the proposed method, the splices would be invisible to the mesh and computation. Upon implementing the proposed method, the computed results are found to agree well with computation using meshes that are much smaller in size. The proposed method thus appears to be effective, accurate and efficient.

The method has been extended to acoustic wave reflection by surfaces with small inhomogeneities with simple geometry. Rectangular and circular shapes are investigated. Essential elements needed to develop modified boundary conditions are established. Further, the method appears to have applications beyond the problems considered in the present study. It is hoped that new insight and a better understanding of finite difference computation could be gained through these new applications.

Appendix A. An estimate on the minimum width of a circumferential splice that can be resolved by the method of wave number truncation

The $\widehat{F}(x)$ function is basically the sum of two slightly displaced $\hat{\mathrm{H}}(x)$ function with opposite sign. This is illustrated in Fig. 20. The slope of the $\hat{\mathrm{H}}(x)$ function is,

$$\frac{d\hat{H}}{dx} = \frac{\sin(\alpha_c x)}{\pi x}.$$

The slope is maximum at point '*A*' where it is equal to α_c/π.

The intersection point '*C*' of Fig. 20 has a value nearly equal to

$$\left(\frac{d\hat{H}}{dx}\right)_{\max} \frac{W}{2} = \frac{W\alpha_c}{2\pi}.$$

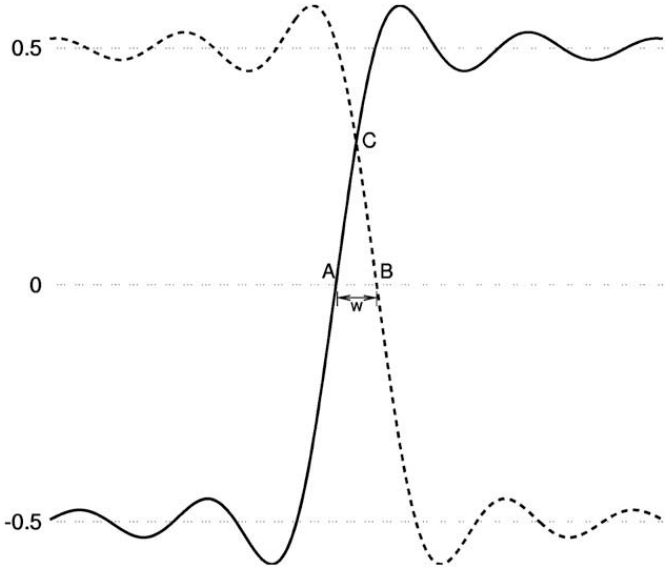

Fig. 20. Formation of the $\widehat{F}(x)$ function by the addition of two opposite slightly displaced $\hat{\mathrm{H}}(x)$ functions.

Because of cancellation between the two $\hat{\mathrm{H}}(x)$ of opposite sign, when adding together the value of the function at point ' C' would be nearly the maximum. Thus

$$\widehat{F}(x)_{\max} \cong \frac{W\alpha_c}{\pi}.$$

In order for the computation to recognize the presence of the splice and be able to resolve it adequately, the height of $\widehat{F}(x)$ should be close to unity. This requires,

$$\frac{W\alpha_c}{\pi} = 1.0 \text{ or } \frac{W}{\Delta x} = \frac{\pi}{\alpha_c \Delta x}.$$

If the 7-point stencil DRP scheme is used for time marching computing, then $\alpha_c \Delta x \cong 1.2$. Thus $W/\Delta x \cong 2.6$. It is, therefore, recommended that the wave number truncation method be used for circumferential splice scattering computation only for splices with width not smaller than 2 mesh spacings.

References

[1] R.E. Motsinger, R.E. Kraft, Design and performance of duct acoustic treatment, in: H.H. Hubbard (Ed.), Aeroacoustics of Flight Vehicles: Theory and Practice, vol. 2, NASA RP-1258, 1995, pp. 165–206.
[2] W. Eversman, Theoretical models for duct acoustic propagation and radiation, in: H.H. Hubbard (Ed.), Aeroacoustics of Flight Vehicles: Theory and Practice, vol. 2, NASA RP-1258, 1995, pp. 101–164.
[3] J.M. Tyler, T.G. Sofrin, Axial flow compressor noise studies, SAE Transactions 70 (1962) 309–332.
[4] A.H. Nayfeh, J.E. Kaiser, D.P. Telionis, Acoustics of aircraft engine-duct system, AIAA Journal 13 (1975) 130–153.
[5] P.E. Doak, P.G. Vaidya, Attenuation of plane wave and higher order mode sound propagation in lined ducts, Journal of Sound and Vibration 12 (1970) 201–224.
[6] D.C. Pridmore-Brown, Sound propagation in a fluid flowing through an attenuation duct, Journal of Fluid Mechanics 4 (1958) 393–406.
[7] S.H. Ko, Sound attenuation in liner rectangular ducts with flow and its application to the reduction of aircraft noise, Journal of the Acoustical Society of America 50 (1971) 1418–1432.
[8] C.K.W. Tam, L. Auriault, The wave modes in ducted swirling flows, Journal of Fluid Mechanics 371 (1998) 1–20.
[9] C.K.W. Tam, J.C. Webb, Dispersion-relation-preserving finite difference scheme for computational acoustics, Journal of Computational Physics 17 (1993) 262–281.
[10] C.K.W. Tam, Computational aeroacoustics: an overview of computational challenges and applications, International Journal of Computational Fluid Dynamics 18 (6) (2004) 547–567.
[11] M. Abramowitz, I.A. Stegun, Handbook of Mathematical Functions with Formulas, Graphs and Mathematical Tables, National Bureau of Standards, Dover Publications, Inc., New York, 1964.
[12] B. Regan, J. Eaton, Modeling the influence of acoustic liners non-uniformities on duct modes, Journal of Sound and Vibration 219 (1999) 859–879.
[13] A. McAlpine, M.C.M. Wright, H. Batard, S. Thezelais, Finite/Boundary Element Assessment of a Turbofan Spliced Intake Liner at Supersonic Fan Operating Conditions, AIAA Paper 2003-3305, 2003.
[14] B.J. Tester, C.J. Powles, N.J. Baker, A.J. Kempton, Scattering of sound by liner splices: a kirchhoff model with numerical verification, AIAA Journal 44 (2006) 2009–2017.
[15] C.K.W. Tam, H. Ju, E.W. Chien, Scattering of acoustic duct modes by axial liner splices, Journal of Sound and Vibration 310 (2008) 1014–1035.
[16] C.K.W. Tam, L. Auriault, Time-domain impedance boundary conditions for computational aeroacoustics, AIAA Journal 34 (1996) 917–923.
[17] Y. Ozyoruk, L.N. Long, M.G. Jones, Time-domain numerical simulation of a flow-impedance tube, Journal of Computational Physics 146 (1998) 29–57.
[18] K.Y. Fung, H. Ju, Broadband time-domain impedance models, AIAA Journal 8 (2001) 1449–1454.
[19] D. Botteldooren, Finite-difference time-domain simulation of low frequency room acoustic problems, Journal of the Acoustical Society of America 98 (1995) 3302–3308.
[20] S. Zheng, M. Zhuang, Verification and validation of time-domain impedance boundary conditions in lined ducts, AIAA Journal 43 (2005) 306–313.

[21] X.D. Li, C. Richter, F. Thiele, Time-domain impedance boundary conditions for surfaces with subsonic mean flows, Journal of Acoustical Society of America 119 (2006) 2665–2676.
[22] S.W. Rienstra, Impedance Models in Time Domain Including the Extended Helmholtz Resonator Model, AIAA Paper 2006-2686, 2006.
[23] H. Ju, K.Y. Fung, Time-domain impedance boundary conditions with mean flow effects, AIAA Journal 39 (2001) 1683–1690.
[24] Y. Reyman, M. Baelmans, W. Desmet, Time-Domain Impedance Formulation Suited for Broadband Simulations, AIAA Paper 2007-3519, 2007.
[25] C.K.W. Tam, K.A. Kurbatskii, Multi-size-mesh multi-time-step dispersion-relation-preserving scheme for multiple-scales aeroacoustics problems, International Journal of Computational Fluid Dynamics 17 (2003) 119–132.
[26] C.K.W. Tam, Z. Dong, Wall boundary conditions for high-order finite difference schemes in computational aeroacoustics, Theoretical and Computational Fluid Dynamics 6 (1994) 303–322.
[27] F.Q. Hu, A Stable, Perfectly matched layer for linearized euler equations in unsplit physical variables, Journal of Computational Physics 173 (2001) 455–480.
[28] F.Q. Hu, Development of PML absorbing boundary condition for computational aeroacoustics: a progress review, Computers and Fluids 37 (2008) 336–348.
[29] C.L. Morfey, Acoustic energy in non-uniform flows, Journal of Sound and Vibration 14 (1971) 159–170.